Applied Catalysis B: Environmental 142–143 (2013) 512–522

Contents lists available at SciVerse ScienceDirect

Applied Catalysis B: Environmental

journal homepage: www.elsevier.com/locate/apcatb

Photocatalytic reduction of carbon dioxide with water vapors over montmorillonite modified TiO_2 nanocomposites

Muhammad Tahir[1], NorAishah Saidina Amin*

Low Carbon Energy Group/Chemical Reaction Engineering Group (CREG), Faculty of Chemical Engineering, Universiti Teknologi Malaysia, 81310 UTM, Skudai, Johor Baharu, Johor, Malaysia

ARTICLE INFO

Article history:
Received 17 January 2013
Received in revised form 8 May 2013
Accepted 22 May 2013
Available online 29 May 2013

Keywords:
CO_2 reduction
Photocatalysis
Montmorillonite
TiO_2 nano-composites

ABSTRACT

Montmorillonite (MMT) modified TiO_2 nanocomposites were synthesized by single step sol–gel method. The samples were characterized by XRD, FE-SEM, HR-TEM, FT-IR, N_2-adsorption–desorption, UV–vis and photoluminescence (PL) spectroscopy. Modification of TiO_2 with MMT controlled the crystal growth and produced anatase phase of delaminated TiO_2 pillared montmorillonite. The size of TiO_2 nanoparticles reduced from 18.73 to 13.87 nm after adding MMT, while the surface area and pore volume increased. The UV–vis results identified blue shift in TiO_2 band gap for the MMT modified samples. In addition, PL spectroscopy revealed significant inhibition in recombination of photogenerated electron–hole pairs. The performance of MMT modified TiO_2 samples for reducing CO_2 with H_2O to hydrocarbon fuels was investigated. The effects of parameters such as MMT loading on TiO_2, H_2O/CO_2 feed ratios, and reaction temperature on TiO_2 photocatalytic activity was studied. Loading MMT on TiO_2 enhanced the performance of TiO_2 and markedly increased CO_2 reduction to C_1–C_3 hydrocarbon fuels. The highest yield rates produced were 441.5 and 103 μmol g cat^{-1} h^{-1} for CH_4 and CO, respectively under UV light irradiations at 20 wt.% MMT loading, reactor pressure of 0.20 bars and 393 K reaction temperature. These results revealed silicate layers of MMT dispersed in the given TiO_2 sol system and vacant d-orbits of the MMT transition metal ions have obvious effect on the photocatalytic activity of TiO_2. The possible pathways and reaction mechanisms of CH_4 and CO productions were also suggested. Thus, MMT is a potentially attractive material to improve TiO_2 as a photocatalyst for application in photocatalytic CO_2 reduction.

© 2013 Elsevier B.V. All rights reserved.

1. Introduction

Global warming effect is associated with increasing concentration of carbon dioxide (CO_2), a greenhouse gas mainly contributed by human activities [1,2]. Recently, numerous efforts are endorsed to reduce CO_2 emission through pre and/or post combustion and also CO_2 through capturing and sequestration. However, these processes are energy intensive, thus uneconomical [3,4]. On the other hand, photoreduction of CO_2 is one of the most promising solutions to both energy crises and global warming, since CO_2 can be reduced to valuable chemicals at relatively low temperature and atmospheric pressure [5,6]. The photocatalytic CO_2 reduction with H_2O to formic acid (HCOOH), formaldehyde (HCHO), methanol (CH_3OH) and methane (CH_4) as the main products was demonstrated three decades ago by Inoue et al. [7]. Since then, various efforts have been taken to design and develop efficient and selective photocatalytic systems for efficient CO_2 photoreduction to value-added chemicals [8–10].

Among various semiconductors, the focus has been on titanium dioxide (TiO_2) as a photocatalyst. TiO_2 has been researched excessively over the past decades due to its encouraging advantages including good photoactivity, relatively low cost, and is abundantly available. It is also chemically/thermally and biologically stable, non-toxic, and possesses higher oxidative potentials [11–13]. In green chemistry, TiO_2 and water (H_2O) are utilized for photocatalytic transformation of CO_2 to hydrocarbon fuels. However, the efficiency of CO_2 reduction with H_2O to CH_4 over TiO_2 is low due to immediate recombination of photogenerated electron–holes pairs [14–16]. On the other hand, the photocatalytic activity of TiO_2 depends on its crystalline structure, particle size, presence of dopant or charge trapping materials, surface area, and surface hydroxyl groups. Therefore, numerous efforts are made to improve its photocatalytic activity for practical applications [17,18].

Recently, mesoporous materials have been under consideration to improve TiO_2 photocatalytic activity because of their higher surface area and more efficient charge trapping capabilities. The

* Corresponding author. Tel.: +60 7 553 5579; fax: +60 7 5588166.
E-mail addresses: bttahir@yahoo.com (M. Tahir), noraishah@cheme.utm.my, profnoraishah@yahoo.com (N.S. Amin).
[1] Permanent address: Department of Chemical Engineering, COMSATS Institute of Information Technology Lahore, Defence Road Off Raiwind Road Lahore, Punjab, Pakistan.

0926-3373/$ – see front matter © 2013 Elsevier B.V. All rights reserved.
http://dx.doi.org/10.1016/j.apcatb.2013.05.054

commonly used materials included clay minerals, activated carbon, graphene oxide, carbon nanotubes, zeolites, and silica [19–24]. Among them, pillared clays constituted a group of mesoporous materials deemed effective to enhance TiO_2 photocatalytic activity. The clay micro-particles are used as support in which TiO_2 nanoparticles are fixed on the surface of a suitable matrix with particle size in the order of micrometers. The clay-TiO_2 heterojunction makes manipulation with photocatalytic material easier for trapping the photogenerated charge particles, improving TiO_2 photoreduction efficiency [25,26]. Moreover, clay materials are low cost, environment friendly, have higher surface area and good adsorption capacity [27,28].

Among pillared clays, montmorillonite (MMT) is a type of natural clays which is multilayered and classified as crystal lattice of 2:1 layered silicates. Its crystal structure consists of layers made up of inner octahedral sheet sandwiched between two outer tetrahedral silicon layers. The octahedral layer composed of aluminum oxide sheet, where some of the aluminum atoms are replaced with magnesium. The difference in valences of Al and Mg creates negative charge distribution within the plane of platelets that are balanced by positive ions, located between platelets or galleries. The MMT silicates layers are held together by relatively weak forces. Water and other relatively polar molecules can enter between the unit layers, causing its lattice to expand. These layers have the tendency to form stacks with a regular van der Waals gap between them called interlayer or gallery. Therefore, silicate layers could disperse during intercalation process and also have unique intercalation/exfoliation characteristics [29].

In order to increase TiO_2 photocatalytic activity, it is hypothesized that MMT shortens the length of charge transport, and improves diffusions of ions over MMT/TiO_2 nanocomposites. The MMT supported TiO_2 nanocomposite can adsorb substances (e.g. CO_2) on its external surfaces or within its interlayers by substitution or interaction. Besides, during TiO_2 intercalation process, MMT functions as barrier, suppressing the formation of crystalline network, and thus minimizing the overwhelming tendency to agglomerate. In this manner, the dispersed TiO_2 over MMT layers improved the surface characteristics with appreciable cation exchange capacity [30].

In photocatalytic CO_2 reduction to higher hydrocarbons, a series of reactions take place. Therefore, efficient materials are needed to achieve decent selectivity and yield of the desired products. The main objective of the present work is to investigate the effect of MMT on photocatalytic activity of TiO_2 nanoparticles for CO_2 photoreduction to hydrocarbons. The photocatalytic CO_2 reduction with H_2O over MMT modified TiO_2 has not been reported yet. It is envisaged that MMT modified TiO_2 nanocomposites synthesized by sol–gel method are able to produce more electrons and holes pairs. The mobility of charges at TiO_2 surface and to some extent vacant d-orbits of transition metals over MMT galleries could promote CO_2 reduction to hydrocarbons.

The photocatalysts were characterized by X-ray diffraction (XRD), field emission scanning electron microscopy (FE-SEM), TEM, FT-IR, N_2 adsorption–desorption measurement, BJH pore size distribution, UV–vis and PL spectroscopy. In addition, the effects of different parameters such as MMT loading, reaction temperature, H_2O/CO_2 feed ratios and possible reaction mechanisms/pathways were also investigated.

2. Experimental

2.1. Sol–gel synthesis of MMT/TiO_2 nanocomposites

TiO_2 nanoparticles and MMT modified TiO_2 nanocomposites were synthesized by sol–gel method using tetra-isopropyl orthotitanate (98%, Merck) as source of titanium (IV), isopropanol (99.7%, QREC), acetic acid (100%, Merck), and MMT (1.44 P, Nanocor). The precursory of titanium solution was prepared with molar ratios; Ti $(C_4H_9O)_4$:15 C_2H_5OH:2CH_3COOH (1 M). Typically, 1 M acetic acid diluted in isopropanol was added drop wise into titanium solution of isopropanol for the hydrolysis process. The solution was stirred vigorously for 24 h at 30 °C. Subsequently, MMT dissolved in isopropanol was added drop by drop into the titanium sol. The process of gelation was continued by stirring the mixture at 30 °C for another 6 h until thick sol was formed. After aging, the slurry was dried in the oven at 80 °C for 24 h under airflow. Finally, the samples were calcined in a muffle furnace at a rate of 5 °C/min up to 500 °C and held at this temperature for 5 h. To synthesize TiO_2 with various concentration of MMT loading, the same procedure was repeated with different MMT loading as per requirements. For comparison, pure TiO_2 nanoparticles were also prepared by applying the same procedure.

2.2. Characterization

In order to determine the structure and crystalinity of the photocatalysts, powder X-ray diffraction (XRD) was performed on Bruker D8 advance diffractometer (Cu-Kα radiation, wavelength λ = 1.54 Å, operated at 40 kV and 40 mA). The scanning rate was 1.2° min^{-1} from 1.5 to 80°. The crystal size was calculated using Scherrer's equation. The surface morphology was examined using field-emission scanning electron microscopy (FE-SEM) with Carl Zeiss Supra 35 VP FE-SEM instrument. The crystallite shape and dispersion of TiO_2 at MMT galleries were observed using TEM and HR-TEM with FEI-Tecni G2 Transmission Electron Microscope (TEM) at EFGO Scientific located at Kulim Hi Tech, Kedah, Malaysia. The infrared spectra were measured at room temperature in the range of 4000–400 cm^{-1} with Spectrum 2000 Explorer Fourier Transformed Infrared (FT-IR) Spectrometer. The nanocomposite powders were dispersed in KBr (90 wt.% of all samples). Textural characterizations of the samples were carried out with a Micromeritics ASAP 2020. The nitrogen adsorption–desorption properties were examined at 77 K. The samples were pre-dried with preliminary heat at 90 °C (1 °C/min) for 1 h to remove moisture and then degassed at 350 °C (10 °C/min) for 8 h prior to measurements. The specific surface area (S_{BET}) of monolayer coverage was determined using Brunauer–Emmett–Teller (BET) method. The pore size distribution was obtained from the adsorption branch of the isotherm by means of Barrett–Joyner–Halenda (BJH) method. UV–vis absorption spectra of the samples were measured with UV-3101PC spectrophotometer. The recombination rate of photogenerated electron–hole pairs was measured by photoluminescence (PL) spectra employing PerkinElmer LS 55 Luminescence Spectrometer.

2.3. Evaluation of photocatalytic activity

The schematic photocatalytic reaction system for reduction of CO_2 with H_2O, illustrated in Fig. 1, consisted of stainless steel chamber having length of 9.5 cm, width of 3.75 cm and total volume of 106 cm^3. The reactor was equipped with a quartz window for the passing of light irradiations. The light source used to activate the photocatalytic reactions was a 500 W mercury lamp for UV irradiations source, having maximum irradiations intensity at 365 nm. The lamp was equipped with water jacket to remove infrared light and heat. The light intensity was measured using online optical process monitor ILT OPM-1D and SED008/W sensor. The reactor was covered with aluminum foil to ensure all the light participated in reactions were from the quartz window only. About 50 mg of powdered photocatalyst was distributed uniformly inside at the bottom of the reactor. The reactor was purged using helium (He)

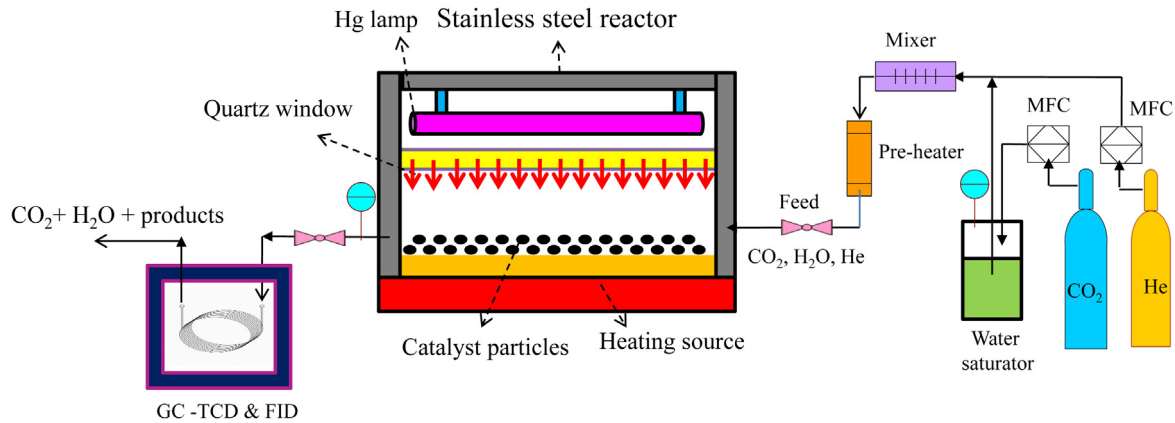

Fig. 1. Schematic of experimental setup for photocatalytic CO_2 reduction with H_2O to hydrocarbons.

flow and checked for leakage at 2 bar pressure for several hours. Compressed CO_2 (99.999%) regulated by mass flow controller (MFC) was bubbled through water bubbler saturator to carry moisture. The concentration of CO_2 was controlled using helium as diluting gas (99.999%). The reactor was purged for an hour using mixtures of CO_2 and helium prior to the start of experiment. The pressure of CO_2 and He (helium) gas mixtures up to 0.20 bars above atmospheric pressure and CO_2 concentration of 20% were maintained throughout the study.

The products were analyzed using an on-line gas chromatograph (GC-Agilent Technologies 6890 N, USA) equipped with thermal conductivity detector (TCD) and flame ionized detector FID (GC/FID/TCD). The gaseous products from the reactor were also taken using gastight syringe (Agilent, 1000 μl) at regular intervals for offline analysis using the same volume as that of online. Furthermore, FID detector was connected with HP PLOT Q capillary column for separation of C_1–C_6 hydrocarbons, alcohols and oxygenated compound while TCD detector consisted of Porapak Q, DC-200, and MS column for separation of C_1–C_6 paraffins and olefins hydrocarbons, CO_2, H_2, O_2, N_2 and CO.

3. Results and discussion

3.1. Characterization of photocatalysts

Fig. 2 presents the XRD patterns of TiO_2, MMT and MMT containing photocatalysts calcined at 500 °C for 5 h. The peaks of TiO_2 revealed pure crystalline and anatase phase. With 10 wt.% MMT loading into TiO_2, pure anatase phase of TiO_2 was produced with wide diffraction peaks. In case of 20 wt.% MMT loading, the diffraction peaks were more wider and weaker than those of photocatalysts prepared without MMT. The MMT XRD pattern showed basal (0 0 1) reflection around $2\theta = 3.70°$. However, MMT containing nanocomposites had dissimilar XRD patterns than the pure MMT. The eminent MMT peak at around $2\theta = 3.70°$, due to layer clays, has disappeared for all TiO_2 containing nanocomposites. This indicates that layered structures of MMT have been destroyed. Furthermore, MMT containing nanocomposites remained original reflections of anatase crystalline phase with no additional peak. However, diffraction peak around $2\theta = 25.50°$ (1 0 1) of MMT modified TiO_2 nanocomposites became weaker and wider and similar trends could be seen for all TiO_2 anatase peaks. These results suggested that layered structure of silicate in MMT has an effect on crystal lattice of MMT containing nanocomposites. This also reveals that addition of MMT in the system allowed the silicate layer of MMT to behave as barrier, which prevented the agglomeration and natural crystallization of TiO_2 sol.

The average crystallite size of TiO_2 nanocomposites was calculated using Scherer's equation according to the (1 0 1) TiO_2 peak (Eq. (1)) [31,32].

$$L = \frac{k\lambda}{\alpha \mathrm{Cos}\theta} \quad (1)$$

where L is the thickness of crystallite (nm), k is a constant depending on crystallite shape (0.90 for this study), λ is the X-ray wavelength (nm), α is full peak width at half max in radians and θ is Bragg's angle of the 2θ peak. The crystallite sizes of TiO_2 and 20% MMT/TiO_2 nanocomposites were 18.7 and 13.87 nm respectively. The crystal size of TiO_2 decreased gradually with MMT loading (Table 1).

The morphology and microscopic structure of 20 wt.% MMT loading photocatalyst was investigated using SEM and FE-SEM as illustrated in Fig. 3(a–d). The SEM images of MMT plates in Fig. 3(a) were almost smooth and uniform in shape. Fig. 3(b) illustrates the FE-SEM images of TiO_2 nanoparticles dispersion on MMT plates. Fig. 3(c and d) exhibits higher magnified FE-SEM images of MMT modified TiO_2 photocatalyst. It is obvious that the MMT layers were destroyed, while TiO_2 nanoparticles were distributed over the entire surface of MMT plates.

The transmission electron microscope (TEM) and high-resolution electron microscopy (HR-TEM) of 20 wt.% MMT/TiO_2 nanocomposite are depicted in Fig. 4(a–d). The TiO_2 nanoparticles are well dispersed over MMT and can be clearly observed from Fig. 4(a). Fig. 4(b) revealed uniform distribution of TiO_2 over MMT

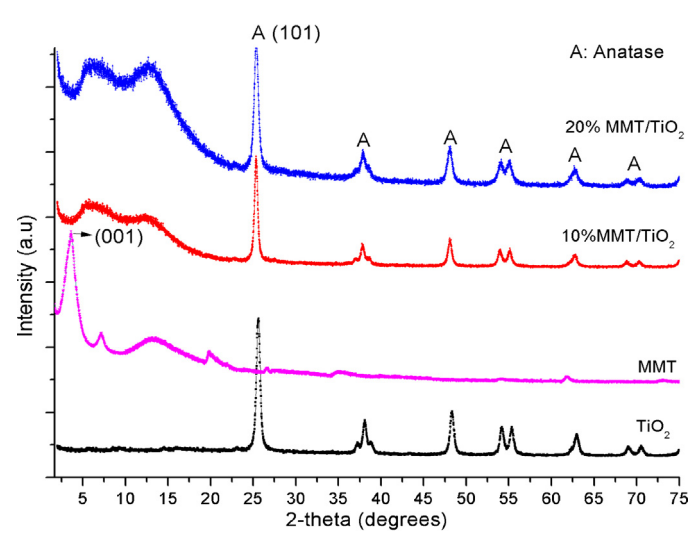

Fig. 2. XRD patterns of anatase TiO_2 nanoparticles, MMT and MMT/TiO_2 nanophotocatalysts.

Table 1
Summary of physiochemical characteristics of TiO_2 nanoparticles and MMT/TiO_2 nanocomposites.

Type of catalyst	Particle size D_{xrd} (nm)	BET surface area S_{BET} ($m^2\,g^{-1}$)	BJH pore volume (cm^3/g)	BJH pore width (nm)
TiO_2	18.73	47.98	0.1347	10.12
MMT/TiO_2[a]	13.87	82.62	0.1578	7.05

[a] MMT = 20 wt.% in TiO_2.

layers and inside galleries, thus confirming efficient intercalation process. It is obvious that the intercalation of TiO_2 nanoparticles into the interlayers of MMT destroyed the ordered structure of MMT, resulting in delaminated TiO_2-pillared montmorillonite. TiO_2 nanoparticles were formed into the interlayers and on the surface of MMT during hydrolysis process. The electron diffraction was performed to identify crystalline structure of TiO_2 as illustrated in Fig. 4(c). Fig. 4(d) shows the lattice fringe spacing of TiO_2 nanoparticle inside MMT galleries having value about to 0.35 nm that clearly relates to anatase phase of TiO_2. Thus, TEM results confirmed efficient distribution of anatase TiO_2 nanoparticles over the silicates layers at MMT galleries.

The infrared (IR) spectra of TiO_2 and its composites are exhibited in Fig. 5. In the spectrum of pure anatase phase of TiO_2, the stretching bend at 1615 cm^{-1} indicated chemisorbed H_2O in TiO_2 is negligible. As shown in the IR spectrum of MMT, the broad band around 3630 cm^{-1} is attributed to Al_2OH group of octahedral layer. The bands around 3460 cm^{-1} and 1630 cm^{-1} can be assigned to —OH stretching and bending vibration of H_2O molecules on the external layer. The peak at 1047 cm^{-1} corresponds to asymmetric vibration of SiO_2 tetrahedral in purified MMT. Several peaks between 1000 and 500 cm^{-1} are attributed to Al-IV tetrahedra [33]. The IR spectrum of MMT modified TiO_2 nanocomposites have obviously changed. The broad band around 3440 cm^{-1} and 1623 cm^{-1} corresponded to stretching vibration of —OH group that are linked with titanium atoms (Ti—OH) and to the bending vibration of H—O—H. These two bands are similar to bare TiO_2 photocatalyst. Furthermore, stretching band at about 1088 cm^{-1} and very weak stretching at around 550 cm^{-1} were observed due to asymmetric stretching vibration of SiO_2 tetrahedra [30,34].

3.2. Adsorption isotherm, surface area and pore structure analysis

Adsorption isotherm, pore size distribution, and cumulative surface area of TiO_2 photocatalysts are depicted in Fig. 6. Fig. 6(a) exhibits the N_2 adsorption–desorption isotherms of pure TiO_2, and 20 wt.% MMT/TiO_2. The isotherms presents typical type IV curve of IUPAC with hysteresis loops, characteristics of mesoporous materials and associated with capillary condensation [35]. The well-defined hysteresis loops with a steep desorption branches and less steep adsorption branches for all materials belongs to H1-type, indicating mesoporous structure of particles [36]. The obvious formation of mesoporous TiO_2 samples without addition of surface directing agents is supposedly due to controlled hydrolysis process at normal temperature in presence of diluted acetic acid.

The initial part of isotherms (at low *P*/*Po*) attributed to monolayer-multilayer adsorption on internal surface of materials. The steep increment at higher *P*/*Po* is due to capillary

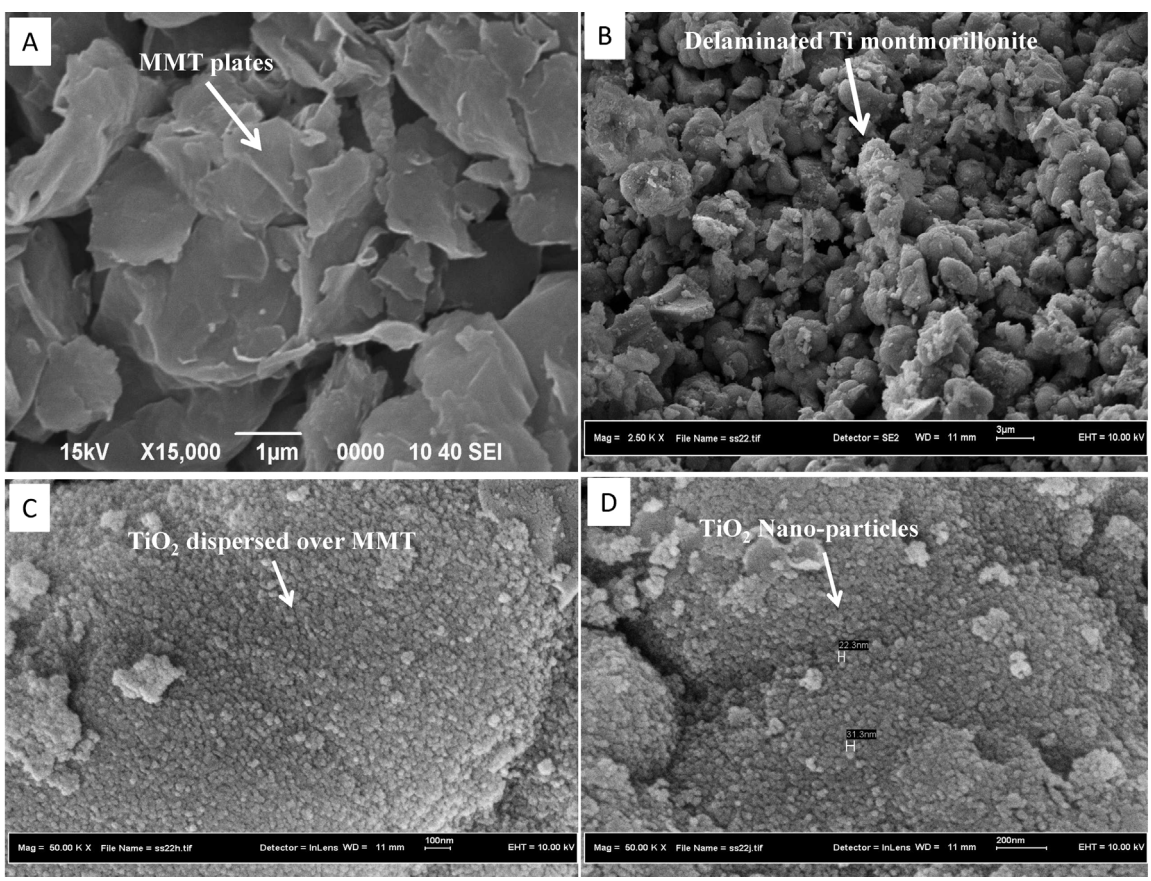

Fig. 3. (a) SEM micrographs of pure MMT plates; (b–d) FES-EM images of delaminated MMT/TiO_2 nanocomposites at different magnifications.

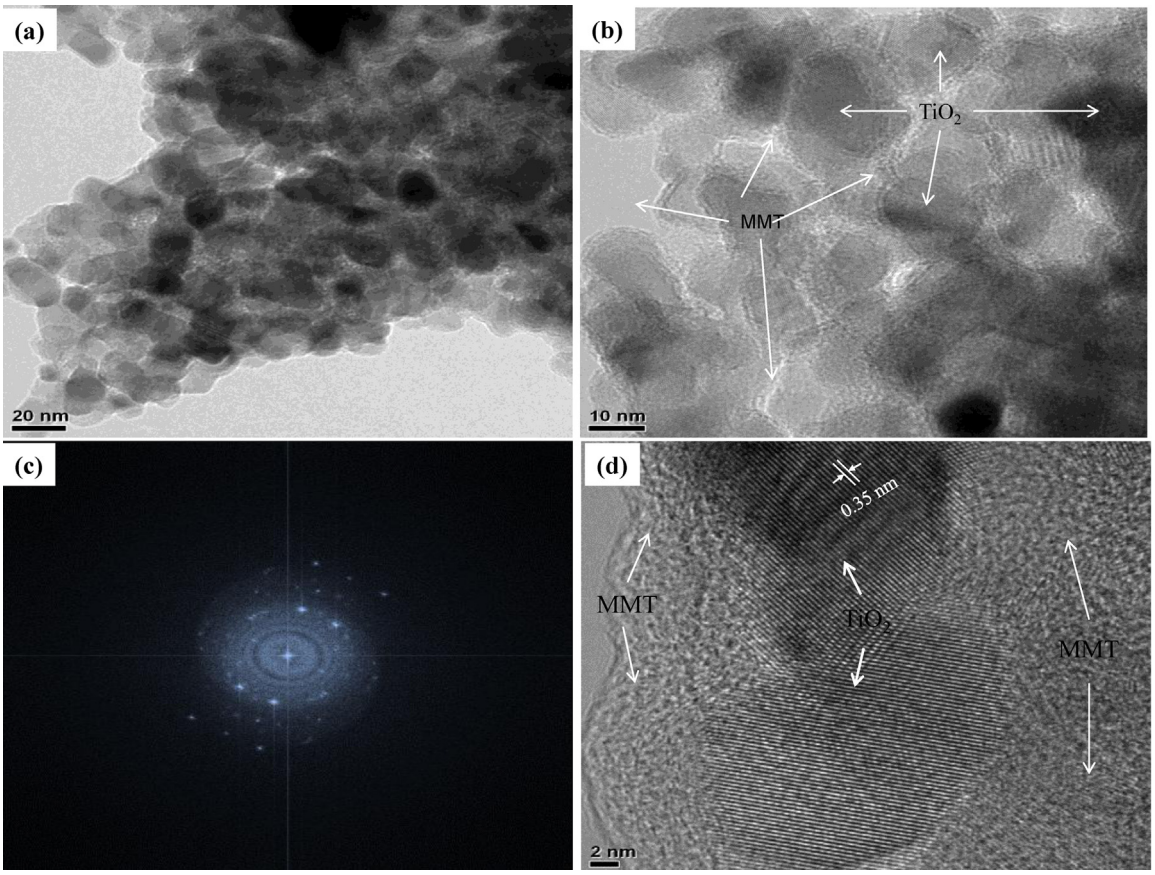

Fig. 4. TEM and HR-TEM images of MMT modified TiO_2 nanocomposite.

condensation within pores followed by saturation as the pores filled with liquid. The binding energy between adsorbate and surface for the first layer known as monolayer is taken as esoteric heat of adsorption. Binding energy of adsorption for all layers subsequent to monolayers can be referred as molar heat of condensation. The monolayer-multilayer is more dominant in TiO_2 in which capillary action started at $P/Po = 0.60$ and 0.55, respectively. However, capillary and condensation action was more prominent in TiO_2/MMT composite and is eminent at P/Po of 0.45.

Fig. 6(b) portrays the BJH pore size distribution of mesoporous TiO_2 and MMT/TiO_2 nanoparticles. The pore sizes distribution curves of all samples were determined from BJH adsorption branch of isotherm, which displays single distribution peak. The TiO_2 pore size distribution peak is in the range of 4–26 nm, while peaks of MMT modified TiO_2 exist in range of 3.5–17 nm, respectively. Furthermore, the pore size distribution narrowed after TiO_2 surface modification and decreased from 14.5 nm to about 9.7 nm for MMT. The reduction in particle size of MMT loaded TiO_2 nanoparticles

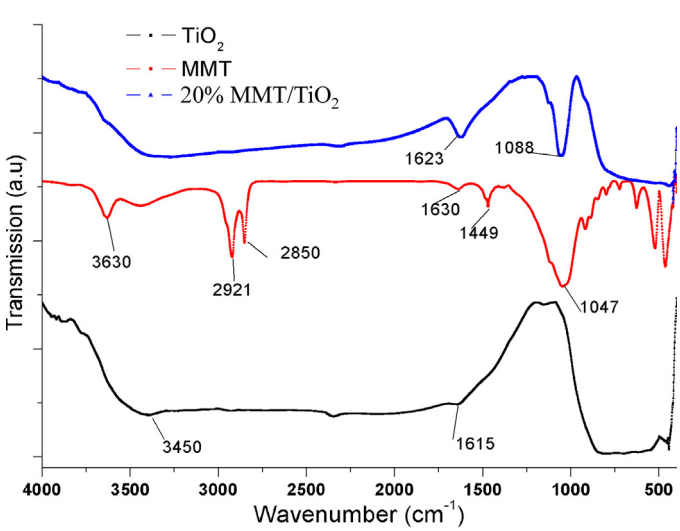

Fig. 5. FT-IR spectra of bare TiO_2, MMT and MMT/TiO_2 (MMT = 20%) photocatalysts.

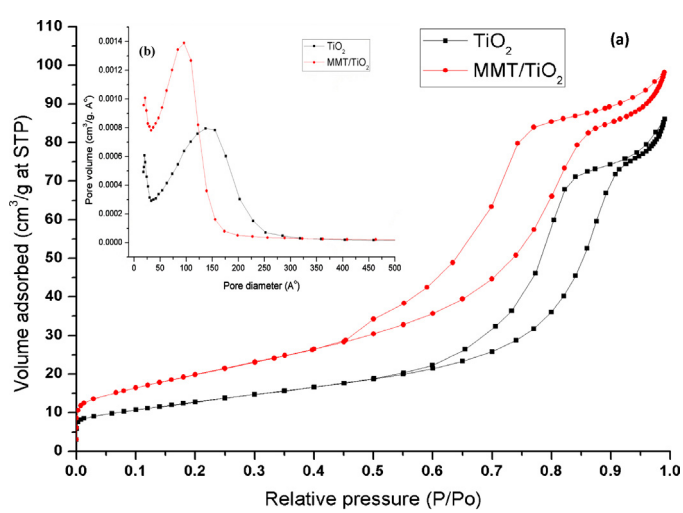

Fig. 6. Adsorption isotherm and pore size distribution of TiO_2 and MMT/TiO_2 nanocomposite: (a) N_2 adsorption–desorption isotherms of TiO_2 nanoparticles and MMT/TiO_2 (MMT = 20%); (b) BJH pore size distributions of corresponding samples.

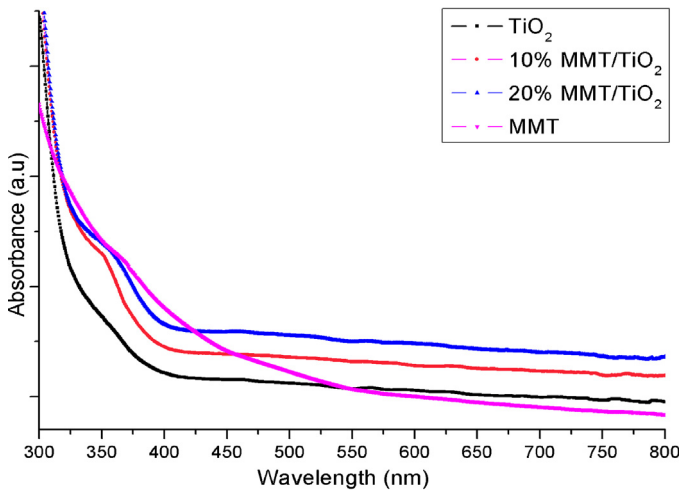

Fig. 7. UV–vis absorption spectra of TiO_2 and MMT modified TiO_2 nanoparticles.

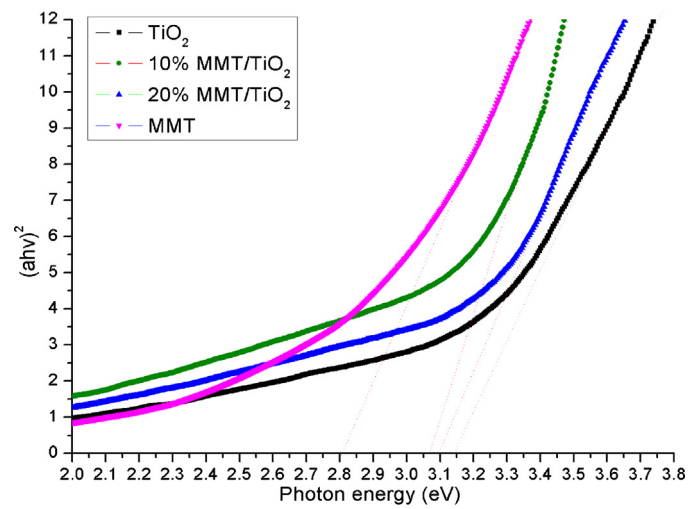

Fig. 8. Band gap energy calculation from absorption spectra of TiO2 nanoparticles and MMT modified TiO_2 nano-particles.

were due to MMT loading. The silicate layer of MMT can behave as barrier, which prevented the agglomeration and natural crystallization of TiO_2 sol.

The surface area, pore volume and pore size of all samples are summarized in Table 1. The surface area was 47.98 $m^2\,g^{-1}$ and 82.62 $m^2\,g^{-1}$ for bare TiO_2 nanoparticles and 20 wt.% MMT loading, respectively. The significant increase in TiO_2 surface area was due to highly dispersed TiO_2 over MMT layered structure and reduced TiO_2 nanoparticle size. The pore size of TiO_2 decreased from 10.12 nm to 7.05 nm with MMT loading due to the strong influence of MMT on crystal growth, resulting in smaller particle size. Similar trends were observed for BJH total pore volumes.

3.3. UV–vis and PL analysis

The UV–vis absorbance spectra of all the photocatalysts and bare MMT are depicted in Fig. 7. The absorption spectrum of TiO_2 nanoparticles appeared around 398 nm, which has red shift compared with intrinsic anatase TiO_2 (energy gap is 3.20 eV). The absorption band edges of MMT modified TiO_2 samples were located at 404 and 408 nm for TiO_2, 10% MMT and 20% MMT into TiO_2, respectively. The light absorption of purified MMT increased to become almost transparent in the wavelength longer than 250 nm. However, in literatures, the absorption band edge for purified MMT (Na-MMT clay) was reported to be transparent in the wavelength range longer than 300 nm [30]. The discrepancy in the results could be because of different types of MMT clays (Ammonium MMT clay in this study). Similar trends for light absorption are reported in literature over MMT K10 [37].

The absorbance spectra were used to calculate the band gap energy (eV) using Tauc equation shown in Eq. (2) [38].

$$\alpha h\nu = A(h\nu - E_g)^{n/2} \quad (2)$$

where α, ν, E_g and A are the absorption coefficient, light frequency, band gap energy and a constant, respectively. The power 'n' characterizes the electronic transition during absorption process. The 'n' value is determined by the type of optical transition of a semiconductor especially having values 1/2, 3/2, 2, and 3 for direct allowed, direct forbidden, indirect allowed and indirect forbidden transitions, respectively. Furthermore, the most common method for the calculation of band gap energy (E_{bg}) involves plotting $(\alpha h\nu)^{n/2}$ vs. $(h\nu)$. The E_{bg} values for all samples were calculated from a plot of $(\alpha h\nu)^2$ versus $(h\nu)$ using direct method as shown in Fig. 8. The E_{bg} estimated from the intercept of the tangents to the plots were 3.12, 3.07 and 3.04 eV for TiO_2, 10 wt.% MMT/TiO_2 and 20 wt.% MMT/TiO_2 respectively. It is obvious that there is a decrease in the band gap energy compared to TiO_2. In addition, there was blue band shift compared to TiO_2. The absorption band gaps were shifted to shorter wavelengths, as the average particle size of TiO_2-MMT was smaller than TiO_2. The layered MMT structure suppressed the growth of TiO_2, and affected the microstructure of TiO_2 and reduced the particle size.

To understand the effect of modifier/sensitizers on the recombination of free electron–holes pairs, photoluminescence (PL) spectra were examined. In general, PL emission spectra can be used to envisage the efficiency of charge carrier trapping, immigration and transfer of charges and to understand the destiny of electron–hole pairs in semiconductor materials. Fig. 9 reveals the PL spectra of bare TiO_2, and MMT modified TiO_2 nanocomposite calcined at 500 °C and excited at 350 nm. MMT modified TiO_2 nanocomposites exhibited PL signal with similar curve shape, demonstrating MMT did not result into new PL phenomenon. The TiO_2 nanoparticles exhibits a wide and strong PL signal in the range of 450–500 nm with the excited wavelength of 350 nm. The lower PL intensity infers lower recombination rate of photogenerated electron and holes pairs. The reduced recombination rate with addition of MMT into TiO_2 is attributed to reduced TiO_2 particle size in

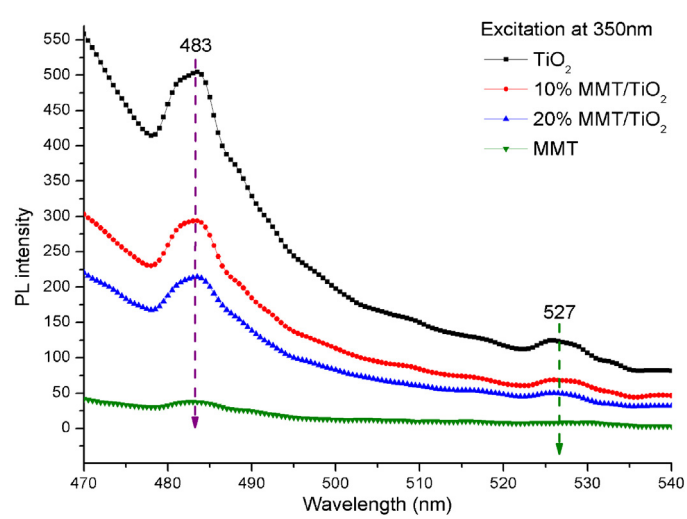

Fig. 9. PL emission spectra of TiO_2 nanoparticles and MMT modified TiO_2 nanocomposite.

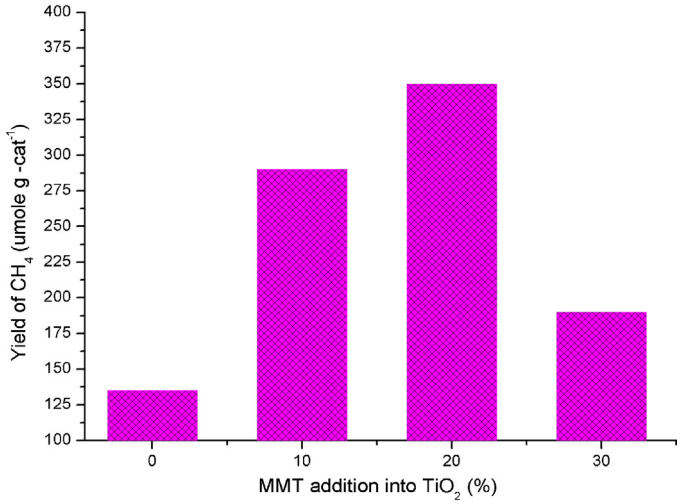

Fig. 10. Effect of MMT loading (wt.%) on TiO_2 photocatalytic activity for photocatalytic CO_2 reduction at reaction temperature 348 K, reaction time 4 h, and P_{H2O} 0.032 bar.

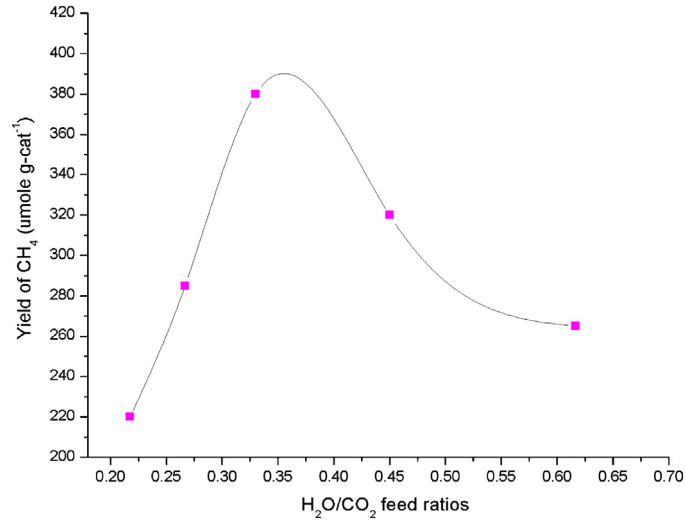

Fig. 11. The yield rate of CH_4 at different feed (H_2O/CO_2) ratios over MMT/TiO_2 photocatalyst, at reaction temperature 348 K, MMT loading 20% and reaction time 4 h.

highly dispersed TiO_2-MMT heterojunction. In addition, the presence of transition metal cations in MMT could also participate in trapping the electrons, resulting in reduced PL intensity [30]. A significant reduction in PL intensity was observed with increasing MMT loading into the TiO_2 structure. This confirmed addition of MMT into TiO_2 efficiently stunted the photogenerated charges (electrons–holes) recombination that occurred at TiO_2 surface.

3.4. Photocatalytic reduction of CO_2 with H_2O

Prior to CO_2 photoreduction experiments, a series of preliminary tests were conducted in the absence of CO_2 and H_2O under UV irradiations for 4 h at 348 K for the following cases; (1) empty reactor and helium, (2) reactor with TiO_2 nanoparticles and helium and (3) MMT/TiO_2 photocatalysts and helium. In all cases, no reaction products were detected confirming no photodecomposition of organic residues in the catalyst, if any. Additional preliminary tests were conducted using H_2O vapors and helium along with photocatalyst under UV irradiations. Again, in either case no carbon-containing compounds were present. These results confirmed photoreduction products were obtained from CO_2 source only. It reiterated that the photocatalytic reduction process require all three components i.e. catalyst, feed (CO_2, H_2O), light source and any carbon containing compound must be produced from CO_2 through photocatalytic reactions.

Fig. 10 illustrates the effect of MMT loading on TiO_2 photocatalytic activity for transformation of CO_2 with H_2O to CH_4. By using pure TiO_2, small amount of CH_4 was produced, while yield was improved by the dispersion of MMT into the TiO_2 structure. The higher yield rate is an evidence that photocatalytic activity of TiO_2 can be enhanced by increasing MMT loading up to an optimum loading of 20 wt.%. MMT loading beyond 20 wt.% lowered the CO_2 photoreduction rate. The difference in the photocatalytic activity of TiO_2 with various MMT loading mainly endorsed effective CO_2 adsorption and efficient charge production and separations over highly dispersed MMT/TiO_2 nanocomposites. Furthermore, excessively high MMT loading may cause charge recombination centers and/or shield the TiO_2 surface from light absorption, both of which reduced the photocatalytic activity.

In addition, photocatalytic CO_2 reduction over pure MMT indicated MMT possessed the photocatalytic activity for the photoreduction of CO_2 with H_2O vapors, but its photocatalytic activity was lesser compared to TiO_2 and MMT/TiO_2 photocatalysts. Chen et al. [30] reported similar results during photocatalytic degradation of sulphorhodamine B under UV–Vis irradiations. MMT photoactivity may be due to the presence of various elements/defects at MMT layered structure and having higher capability of light absorption.

Fig. 11 exhibits the relationship between CH_4 yield and H_2O/CO_2 ratios in initial feed stream keeping all other parameters fixed. With the MMT loading of 20 wt.% in TiO_2, CH_4 yield increased with increasing H_2O/CO_2 feed ratio as the large concentration of H_2O molecules adsorbed at the catalyst surface to react with CO_2, resulting in high CO_2 photoreduction. Furthermore, CO_2 and H_2O molecules were competitively activated by the charge transfer excited complexes and the values of H_2O/CO_2 ratios influenced the selectivity for the formation of the desired products [39]. The highest CH_4 yield was achieved at H_2O/CO_2 ratio = 0.35. Further increment in the feed ratios lowered the CO_2 photoreduction activity. This phenomenon was likely due to adsorption competition between CO_2 and H_2O molecules on the active sites of MMT/TiO_2 nanocomposites during photoreduction process. In presence of MMT, TiO_2 became super hydrophilic, when irradiated by UV light and H_2O molecules would cover most of the catalyst surface. At high H_2O/CO_2 feed ratio, CO_2 would have to compete with H_2O for the active sites in order to react with adsorbed H_2O. Thus, reducing H_2O pressure or raising CO_2 pressure would increase CO_2 reduction rate. On the other hand, when H_2O pressure was much lower than that of CO_2, less H_2O content would reduce the reaction rate. Therefore, an optimum H_2O/CO_2 feed ratio could enhance the CO_2 conversion efficiency. Similar findings have been reported in literature during photocatalytic CO_2 with H_2O vapors using various TiO_2 based photocatalysts [40].

The effect of reaction temperature on photocatalytic CO_2 reduction at 20 wt.% MMT loading and H_2O/CO_2 ratio = 0.35 is shown in Fig. 12. It is obvious that CH_4 yield increased with reaction temperature. In general, higher temperature gave positive effects on photocatalytic reactions particularly in gas phase reactions and can accelerate the reaction rate. During photocatalysis process, simultaneous adsorption and desorption processes occurred at catalyst surface and rate of reaction depends on the efficiency of these processes. The increased in temperature increased desorption of reaction products from the catalyst surface and enhanced the chance of efficient collisions between the charge transfer excited state $[Ti^{3+} - O^{-}]^{*}$ species and reactant molecules [10]. Moreover,

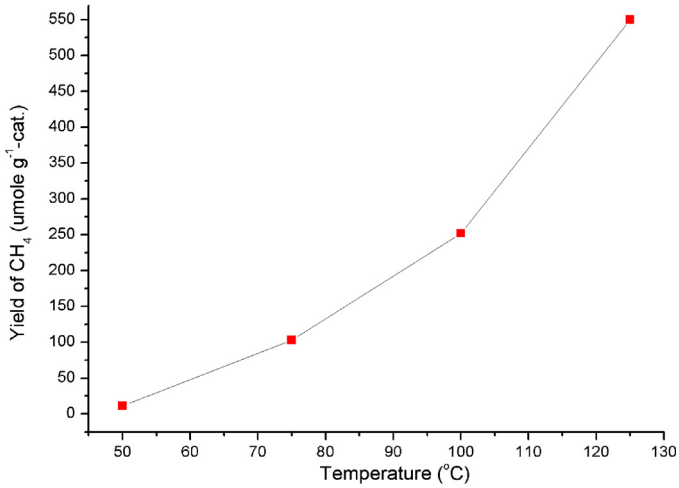

Fig. 12. Effects of temperature on photocatalytic CO_2 reduction over MMT/TiO_2 photocatalyst at MMT loading 20%, reaction time 2 h, and P_{H2O} of 0.042 bar.

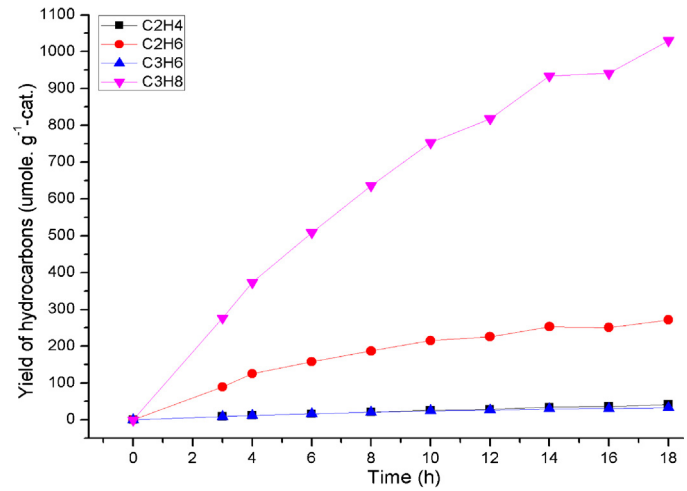

Fig. 14. Photocatalytic CO_2 reduction with H_2O to higher hydrocarbons over MMT modified TiO_2 photocatalyst at reaction temperature 393 K, MMT loading 20%, and P_{H2O} 0.042 bar.

in heterogeneous photocatalysis, reaction rates are usually determined by applying the principal of law of mass action in terms of surface concentrations. During desorption process at elevated temperature, diffusion of CO_2 toward catalyst surface could be increased to occupy vacant sites, thus probability of adsorption increases, resulting in higher reaction rates [41]. Furthermore, the significant increase in reaction rate by increasing temperature indicated that activation energy decreased during course of reaction. Saladin and Alxneit [42] investigated the effect of temperature on photochemical reduction of CO_2 with H_2O in gas phase over TiO_2 and reported similar trends.

The effects of irradiation time on photocatalytic CO_2 reduction using MMT modified TiO_2 photocatalysts were investigated for the duration of 0–24 h as depicted in Figs. 13 and 14. From the GC analysis, six products namely methane (CH_4), carbon monoxide (CO), ethane (C_2H_6), ethylene (C_2H_4), propane (C_3H_8), and propylene (C_3H_6) were obtained. As shown in Fig. 13, CH_4 and CO were the main products and their yield rates increased gradually with reaction time. Significant amount of C_2H_4, C_2H_6, C_3H_6 and C_3H_8 were also produced over MMT modified TiO_2 (Fig. 14). In addition, all products were produced continuously during the entire experiment in presence of MMT/TiO_2 and steady state was not achieved

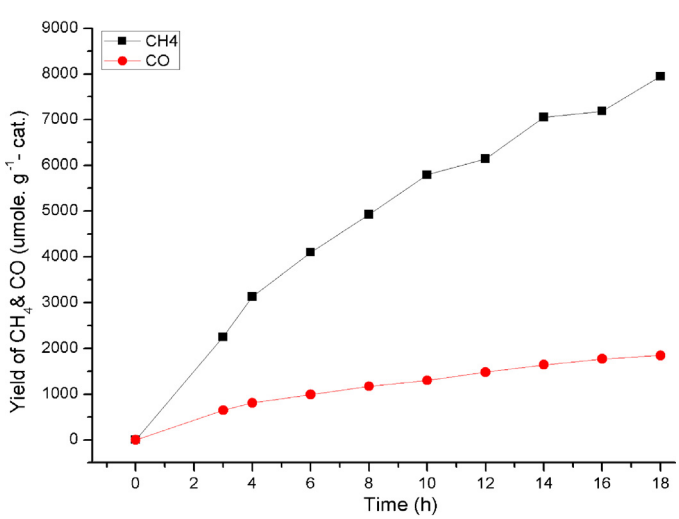

Fig. 13. Photocatalytic CO_2 reduction with H_2O to CH_4 and CO over MMT modified TiO_2 photocatalyst at reaction temperature 393 K, MMT loading 20%, and P_{H2O} 0.042 bar.

even after 24 h of irradiations. In case of TiO_2, all the products were generated for the first 14 h (figure not shown here) before reaching steady-state condition. These results demonstrated MMT is a promising material for enhancing photoreduction efficiency as it provided more stability and reactivity to TiO_2. Similar finding has been reported during photocatalytic CO_2 reduction with H_2O over CdS- MMT photocatalyst [38].

However, photo-oxidation products such as oxygen (O_2) were not detected in the gaseous product mixtures. O_2 was also not reported in previous studies during photocatalytic CO_2 reduction with H_2O over TiO_2 based photocatalysts [42]. For this, several possibilities exist; nevertheless, it has also been reported that O_2 together with oxygen-containing compound such as CO could have been photo-adsorbed, blocking the active sites and hindering the diffusion of intermediates on the catalyst surface. Based on other related studies [43,44] which detected O_2 in the reaction products, it is likely that O_2 was also formed in this study but photo-adsorption prevented it to be detected by MS column due to low concentration in gaseous product mixtures as similarly reported by other researchers [42].

The average yield rates of CO_2 transformation products over TiO_2 and MMT modified TiO_2 photocatalysts are compared in Fig. 15. The presence of MMT plays an important role in efficient reduction of CO_2 to different paraffins and olefins. The total products significantly increased after MMT loading into TiO_2. Over MMT modified TiO_2, the largest yield of CH_4 was 441.5 μmol g cat^{-1} h^{-1}; 12 folds higher than pure TiO_2. In addition, CO was the second largest product with yield rate of 103 μmol g cat^{-1} h^{-1}. Significant amounts of C_1–C_3 hydrocarbons were also produced, which were not observed in bare TiO_2. The photocatalytic performance of MMT modified TiO_2 was in the order of (μmole per g of catalyst) $CH_4 > CO > C_3H_8 > C_2H_6 > C_2H_4 > C_3H_6$. Various sites of MMT modified TiO_2 nanocomposites acted as oxidizing/reducing centers, providing electron to CO_2 as well as accepting electrons from H_2O vapors in reaction mixture. Therefore, MMT served as electron traps to inhibit recombination of electron–holes pairs. On the other hand, surface hydroxyl (OH) groups over MMT/TiO_2 increased more CO_2 adsorption, which can enhance photocatalytic activity. In general, higher photoactivity of TiO_2 in the presence of MMT can be attributed to the followings:

(1) The layered structure of silicate in MMT controls the crystal growth, resulting in smaller TiO_2 particle size. The TiO_2 with smaller particle sizes have higher photocatalytic activity due to

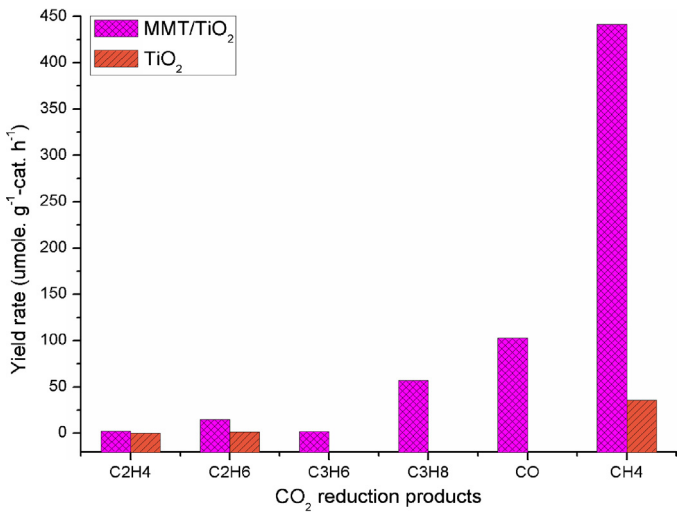

Fig. 15. Average production rate of all hydrocarbon products over MMT modified TiO_2 photocatalyst at reaction temperature 393 K, MMT loading 20%, and P_{H2O} 0.042 bar.

more electrons being produced and are more mobile on TiO_2 surface. The smaller particle sizes also hindered recombination of electron–hole pairs.

(2) The delaminated TiO_2 pillared montmorillonite has higher surface area because of its exfoliated structure. Due to this, there is possibility of higher CO_2 adsorption, efficient light harvesting/capturing and more photocatalytic reaction active sites, resulting in improved photo-efficiency.

(3) In the galleries of MMT, there are possible d-orbits vacant cations that could trap electrons during TiO_2 photocatalysis, and possibly enhanced photocatalytic activity.

3.5. Mechanism of photocatalytic CO_2 reduction with H_2O vapors

During photocatalytic CO_2 reduction with H_2O vapors under UV lightlight irradiations, CO, CH_4 and some higher hydrocarbons (attributed to paraffins and olefins) were detected. In these photocatalysis reactions, CO_2 reduced and H_2O oxidized. In general, the first step in photocatalysis was the production of electron–holes pairs when light striked on the TiO_2 surface. The electrons (e^-) transferred from the TiO_2 conduction band for the photoreduction of CO_2, yielding $^{\bullet}CO_2^-$ radicals. On the other hand, holes (h^+) were transferred to H_2O initiating its photooxidation, yielding hydrogen ions (H^+) and hydroxyal radical ($^{\bullet}OH$) and further oxidized with $^{\bullet}OH$ radicals for the production of O_2 and H^+ [44]. The $^{\bullet}H$ radicals originated during reduction of proton reacted with carbon radicals on the catalyst surface to produce intermediates $^{\bullet}CH_2$ and $^{\bullet}CH_3$ radicals and finally CH_4 and higher hydrocarbons. All possible reaction steps during photocatalytic CO_2 reduction with H_2O are explained by Eqs. (3–9).

$$TiO_2 \xrightarrow{E_{ph} \geq E_{bg}} e^-_{cb}(TiO_2) + h^+_{vb}(TiO_2) \quad (3)$$

$$MMT(metals) + e^- \rightarrow MMT(metals)(e^-) \quad (4)$$

$$H_2O + h^+ \rightarrow {}^{\bullet}OH + H^+ \xrightarrow{e^-, H_2O} {}^{\bullet}H + O_2 \quad (5)$$

$$CO_2 + e^- \rightarrow {}^{\bullet}CO_2^- \xrightarrow{{}^{\bullet}H} CO + OH^- \quad (6)$$

$$CO + e^- \rightarrow {}^{\bullet}CO^- \xrightarrow{{}^{\bullet}H} {}^{\bullet}C + OH^- \quad (7)$$

$$^{\bullet}C + {}^{\bullet}H \rightarrow {}^{\bullet}CH \xrightarrow{{}^{\bullet}H} {}^{\bullet}CH_2 \xrightarrow{{}^{\bullet}H} {}^{\bullet}CH_3 \xrightarrow{{}^{\bullet}H} CH_4 \quad (8)$$

$$n{}^{\bullet}CH_2 + m{}^{\bullet}CH_3 \xrightarrow{{}^{\bullet}H} C_2H_4 + C_2H_6 + C_3H_6 + C_3H_8 \quad (9)$$

During TiO_2 photocatalysis, large number of electrons would be produced due to highly dispersed nanosize TiO_2 particles over MMT layers. At the same time, electron transition of vacant d-orbits of metal ions on MMT supposedly trap charge particles (Eq. (4)) resulting in more electron production and mobility over TiO_2 surface for CO_2 reduction.

Since all of the above products were detected experimentally, CH_4 was confirmed to be produced from methyl radicals ($^{\bullet}CH_3$). These radicals were directly dependent on the formation of the intermediate product, CO. The production of higher CH_4 yield rate (Eq. (8)) and other higher hydrocarbons (Eq. (9)) also confirmed H_2 during water oxidation and carbon radicals during CO_2 reduction were produced excessively to support these reactions (Eqs. (8) and (9)). Based on such observations, it could be assumed that large number of electron–hole pairs were produced over the surface of MMT modified TiO_2, yielding CO as intermediate product, and finally C_1–C_3 hydrocarbons. Similar observations were reported by Saladin and Alxneit [42] during gas phase reduction of CO_2 with H_2O over TiO_2 surface. Furthermore, higher hydrocarbons yield rates has confirmed that the reactions in Eqs. (8)–(9) were more favorable over the MMT/TiO_2 surface. From the reaction summary and in view of the above observations, there is higher probability for producing hydrocarbons by improving the TiO_2 oxidation and reduction potentials. However, further investigations are required to understand the detailed reaction mechanism for predicting possible reaction products.

The photocatalytic CO_2 transformation to CO and CH_4 over MMT modified TiO_2 could be further explained using energy band theory, which is based on the relative positions of conductance band, valance band and oxidation potentials. In general, photo-excited electrons can be consumed effectively, if the reduction potential of the reaction is lower than the conductance band potential of the semiconductor [45]. The possible reactions that can occur during photocatalytic CO_2 with H_2O to produce CO and CH_4 in terms of thermodynamic reduction potentials versus normal hydrogen electrode (NHE) can be described by reactions in Eqs. (10)–(13) [46–48].

$$CO_2 + 2H^+ + 2e^- \rightarrow CO + H_2O \quad E^o = -0.48\,V \quad (10)$$

$$2H^+ + 2e^- \rightarrow H_2 \quad E^o = -0.41\,V \quad (11)$$

$$CO_2 + 8H^+ + 8e^- \rightarrow CH_4 + 2H_2O \quad E^o = -0.24\,V \quad (12)$$

$$2H_2O + 4h^+ \rightarrow 4H^+ + O_2 \quad E^o = +0.82\,V \quad (13)$$

The conductance band potential of TiO_2 is $E_{CB} = -0.50$ V at pH 7. CO was observed due to the reduction potential of $E^o(CO_2/CO) = -0.48$ V was lower than −0.5 V (conductane band of TiO_2). For CO_2 reduction to CH_4, the lower reduction potential difference ($E^o(CO_2/CH_4) = -0.24$ V) also drove the reaction. Although the reduction potential of Eq. (10) is much lower than Eq. (12), eight electrons are required to produce CH_4 compared to only two for CO. Thus, significant yield rate of CO was also observed in the gaseous product mixtures.

On the basis of XRD studies, TEM observations and reaction mechanism, a schematic reaction scheme is depicted in Fig. 16. During photocatalyitc CO_2 reduction, a series of reaction takes place to get valuable hydrocarbons, as portrayed in Fig. 16(a). Because of the efficient intercalation process, TiO_2 nanoparticles could penetrate and distribute over MMT layers and inside galleries to form delaminated TiO_2 pillared montmorillonite as portrayed in Fig. 16(b). Under light irraditions, there was efficient production and absoprtion of electrons over the MMT/TiO_2 nanocomposites surface. Subsequently, electron transferred from the conductance

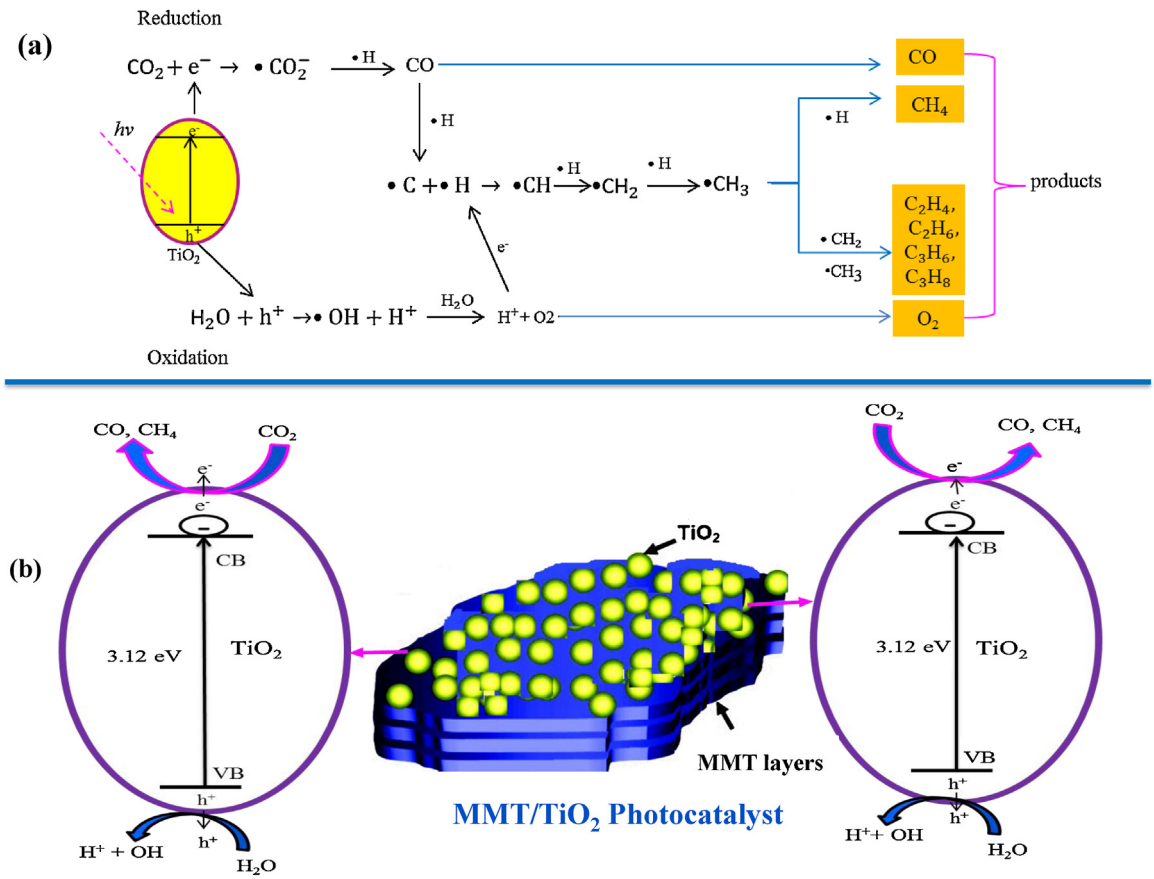

Fig. 16. (a) Reaction scheme for the production of CO, CH_4 and hydrocarbons during photocatalytic CO_2 reduction and H_2O oxidation; (b) schematic structure of MMT/TiO_2 nanocomposites and possible reaction mechanism for photocatalytic reduction of CO_2 with H_2O.

band of TiO_2, trapped by CO_2 molecules led to CO_2 reduction process. A series of reactions take place over delaminated TiO_2 pillared montmorillonite for possible higher yield rates of C_1–C_3 paraffins and olefins. The higher CH_4 and significant C_1–C_3 hydrocarbons yield rates over MMT/TiO_2 nanocomposites confirmed MMT as an efficient material for conversion of CO_2 to valuable C_1–C_3 hydrocarbons. More importantly, production of C_1–C_3 hydrocarbons have been reported for the first time over the MMT/TiO_2 photoctalyst.

4. Conclusions

MMT modified TiO_2 photocatalysts were synthesized by sol–gel single step method and for the first time were tested for the activity of photocatalytic CO_2 reduction with H_2O. When MMT dispersed into TiO_2 solution, the silicate layer of MMT behaved as a barrier to prevent agglomeration formation. The layered MMT structure was destroyed during intercalation process and formed delaminated TiO_2 pillared montmorillonite. The average particle size of MMT modified TiO_2 was smaller than the bare TiO_2 nanoparticles. Therefore, loading MMT into TiO_2 structure increased surface area, reduced particle size and enabled efficient charge separation. Significant enhancement of CO_2 photoreduction with H_2O to CO and C_1–C_3 hydrocarbons was observed over MMT modified TiO_2 compared to bare TiO_2 under UV irradiations. The effects of MMT loading, H_2O/CO_2 feed ratios and reaction temperature was also investigated to maximize conversion efficiency. An optimum H_2O/CO_2 feed ratio = 0.35 gave the highest yield for CH_4. The temperature also improved the photoactivity by enhancing CO_2 adsorption rate and accelerating photogenerated species. The highest yield rates of CH_4 and CO as main products were 441.5 and 103 μmol g cat^{-1} h^{-1}, respectively. The mechanism of CO_2 photoconversion with H_2O to CH_4 and CO can be explained by energy band theory. MMT seems a promising material to improve the effectiveness and feasibility of TiO_2 as a photocatalyst for CO_2 photoreduction for carbon management applications.

Acknowledgements

The authors would like to extend their deepest appreciation to the Ministry of Higher Education (MOHE) and Universiti Teknologi Malaysia for financial support of this research under LRGS (Long-term Research Grant Scheme), and RUG (Research University Grant).

References

[1] X. Li, H. Liu, D. Luo, J. Li, Y. Huang, H. Li, Y. Fang, Y. Xu, L. Zhu, Chem. Eng. J. 180 (2012) 151–158.
[2] Y.G. Wang, B. Li, C.L. Zhang, L.F. Cui, S.F. Kang, X. Li, L.H. Zhou, Appl. Catal. B: Environ. 130 (2013) 277–284.
[3] Y. Li, W.N. Wang, Z.L. Zhan, M.H. Woo, C.Y. Wu, P. Biswas, Appl. Catal. B: Environ. 100 (2010) 386–392.
[4] Q.Y. Zhang, Y. Li, E.A. Ackerman, M. Gajdardziska-Josifovska, H.L. Li, Appl. Catal. A: Gen. 400 (2011) 195–202.
[5] K. Teramura, S.-i. Okuoka, H. Tsuneoka, T. Shishido, T. Tanaka, Appl. Catal. B: Environ. 96 (2010) 565–568.
[6] K. Mori, H. Yamashita, M. Anpo, RSC Adv. 2 (2012) 3165.
[7] T. Inoue, F. Akira, K. Satoshi, H. Kenichi, Nature 277 (1979) 637–638.
[8] M. Kitano, M. Matsuoka, M. Ueshima, M. Anpo, Appl. Catal. A: Gen. 325 (2007) 1–14.
[9] G. Centi, S. Perathoner, Catal. Today 148 (2009) 191–205.
[10] Q.H. Zhang, W.D. Han, Y.J. Hong, J.G. Yu, Catal. Today 148 (2009) 335–340.
[11] X. Wang, T.-T. Lim, Appl. Catal. B: Environ. 100 (2010) 355–364.
[12] G.L. Chiarello, E. Selli, L. Forni, Appl. Catal. B: Environ. 84 (2008) 332–339.

[13] A. Kleiman, A. Marquez, M.L. Vera, J.M. Meichtry, M.I. Litter, Appl. Catal. B: Environ. 101 (2011) 676–681.
[14] A. Di Paola, E. Garcia-Lopez, G. Marci, L. Palmisano, J. Hazard. Mater. 211–212 (2012) 3–29.
[15] A.R. Khataee, M.B. Kasiri, J. Mol. Catal. A: Chem. 328 (2010) 8–26.
[16] N.M. Dimitrijevic, B.K. Vijayan, O.G. Poluektov, T. Rajh, K.A. Gray, H. He, P. Zapol, JACS 133 (2011) 3964–3971.
[17] S. Krejcíkova, L. Matejova, K. Kocí, L. Obalova, Z. Matej, L. Capek, O. Solcova, Appl. Catal. B: Environ. 111–112 (2012) 119–125.
[18] T.T. Le, M.S. Akhtar, D.M. Park, J.C. Lee, O.B. Yang, Appl. Catal. B: Environ. 111 (2012) 397–401.
[19] B. Damardji, H. Khalaf, L. Duclaux, B. David, Appl. Clay Sci. 44 (2009) 201–205.
[20] C.-C. Yang, J. Vernimmen, V. Meynen, P. Cool, G. Mul, J. Catal. 284 (2011) 1–8.
[21] M. Takeuchi, S. Dohshi, T. Eura, M. Anpo, J. Phys. Chem. B 107 (2003) 14278–14282.
[22] Y. Min, K. Zhang, W. Zhao, F. Zheng, Y. Chen, Y. Zhang, Chem. Eng. J 193–194 (2012) 203–210.
[23] K. Ikeue, H. Yamashita, M. Anpo, T. Takewaki, J. Phys. Chem. B 105 (2001) 8350–8355.
[24] M. Anpo, H. Yamashita, K. Ikeue, Y. Fujii, S.G. Zhang, Y. Ichihashi, D.R. Park, Y. Suzuki, K. Koyano, T. Tatsumi, Catal. Today 44 (1998) 327–332.
[25] Y. Kameshima, Y. Tamura, A. Nakajima, K. Okada, Appl. Clay Sci. 45 (2009) 20–23.
[26] C. Wang, H. Shi, P. Zhang, Y. Li, Appl. Clay Sci. 53 (2011) 646–649.
[27] K.G. Bhattacharyya, S.S. Gupta, Chem. Eng. J. 136 (2008) 1–13.
[28] K. Bhattacharyya, Appl. Clay Sci. 41 (2008) 1–9.
[29] D.R. Paul, L.M. Robeson, Polymer 49 (2008) 3187–3204.
[30] K. Chen, J. Li, J. Li, Y. Zhang, W. Wang, Colloids Surf. Physicochem. Eng. Aspects 360 (2010) 47–56.
[31] H. Liu, H.K. Shon, X. Sun, S. Vigneswaran, H. Nan, Appl. Surf. Sci. 257 (2011) 5813–5819.
[32] S.B. Kondawar, S.R. Thakare, N.S. Bhave, D.K. Burghate, Int. J. Nanosci. 10 (2011) 1231–1235.
[33] L. Bouna, B. Rhouta, M. Amjoud, F. Maury, M.C. Lafont, A. Jada, F. Senocq, L. Daoudi, Appl. Clay Sci. 52 (2011) 301–311.
[34] L.L. Yuan, D.D. Huang, W.N. Guo, Q.X. Yang, J. Yu, Appl. Clay Sci. 53 (2011) 272–278.
[35] A.A. Ismail, D.W. Bahnemann, S.A. Al-Sayari, Appl. Catal. A: Gen. 431 (2012) 62–68.
[36] S. Liu, E.Y. Guo, L.W. Yin, J. Mater. Chem. 22 (2012) 5031–5041.
[37] T.S. Wu, K.X. Wang, G.D. Li, S.Y. Sun, J. Sun, J.S. Chen, ACS Appl. Mater. Interfaces 2 (2010) 544–550.
[38] P. Praus, O. Kozak, K. Koci, A. Panacek, R. Dvorsky, J. Colloid Interface Sci. 360 (2011) 574–579.
[39] K. Ikeue, S. Nozaki, M. Ogawa, M. Anpo, Catal. Today 74 (2002) 241–248.
[40] J.C.S. Wu, H.M. Lin, C.L. Lai, Appl. Catal. A: Gen. 296 (2005) 194–200.
[41] S.S. Tan, L. Zou, E. Hu, Catal. Today 131 (2008) 125–129.
[42] F. Saladin, I. Alxneit, J. Chem. Soc., Faraday Trans. 93 (1997) 4159–4163.
[43] M. Anpo, H. Yamashita, Y. Ichihashi, S. Ehara, J. Electroanal. Chem. 396 (1995) 21–26.
[44] S.S. Tan, L. Zou, E. Hu, Catal. Today 115 (2006) 269–273.
[45] X.Y. Yang, T.C. Xiao, P.P. Edwards, Int. J. Hydrogen Energy 36 (2011) 6546–6552.
[46] A.H. Yahaya, M.A. Gondal, A. Hameed, Chem. Phys. Lett. 400 (2004) 206–212.
[47] Y. Zhou, Z. Tian, Z. Zhao, Q. Liu, J. Kou, X. Chen, J. Gao, S. Yan, Z. Zou, ACS Appl. Mater. Interfaces 3 (2011) 3594–3601.
[48] C. Zhao, A. Krall, H. Zhao, Q. Zhang, Y. Li, Int. J. Hydrogen Energy 37 (2012) 9967–9976.